Nanoscale

ROYAL SOCIETY OF CHEMISTRY

PAPER

View Article Online
View Journal | View Issue

Cite this: *Nanoscale*, 2020, **12**, 19655

Cubic nano-silver-decorated manganese dioxide micromotors: enhanced propulsion and antibacterial performance†

Wenjuan Liu, *[a,b] Hongbin Ge,[a] Xiaoyong Ding,[a] Xiaolong Lu,*[c] Yanan Zhang[a,b] and Zhongwei Gu[a,b]

Received 31st August 2020,
Accepted 11th September 2020

DOI: 10.1039/d0nr06281b

rsc.li/nanoscale

The increasing threat of antibiotic-resistant bacterial strains represents the current antibacterial dilemma and requires novel bactericidal treatment to circumvent this problem. In this work, an efficient strategy for killing bacteria using PEDOT/MnO_2@Ag micromotors is reported based on the intense motion-induced convection and excellent sterilization ability of silver (Ag) ions. A distinctive inner surface structure with cubic Ag nanoparticle growth and dispersion in the MnO_2 layer was constructed by simple cathodic co-electrodeposition. Due to the synergistic catalytic reaction of both MnO_2 and Ag, the micromotors can rapidly swim in very low concentrations of hydrogen peroxide (H_2O_2). The antibacterial efficiency of the micromotors was evaluated with the *Escherichia coli* (*E. coli*) model. The continuous movement of micromotors, corresponding to violent mass transfer, along with the on-the-fly release of silver ions, greatly enhanced bacteria killing efficacy, with about 14% increase in bacterial death in 0.2% H_2O_2 solution as compared to no motors. Such proposed micromotors could be ideal candidates for combating antibiotic-resistant bacteria in the fields of biomedical and environmental applications.

Introduction

Bacterial infection has been a long-lasting threat to human health and results in significant number of deaths every year.[1,2] Antibiotics were invented to circumvent this problem but antibiotic resistance greatly hinders their further applications. To respond to the current antibacterial dilemma, antibiotic-free strategies are required with targeted and destructive antibacterial activity against pathogenic bacteria, minimizing the spread of antibiotic-resistant bacteria. Recent advances in nanotechnology have opened up a new avenue for addressing this issue by employing the unique features of nanomaterials, and remarkable success has been achieved in antibacterial applications. Through the high specific surface area and other intriguing properties of nanomaterials, organically combining antibacterial materials with nanotechnology greatly improves the antibacterial performance and efficiency.[3] For instance, photocatalytic metallic oxides (Fe_3O_4, TiO_2) made into nanometer grade, can obtain a better antibacterial effect due to their increased specific surface area, excellent reactive oxygen species (ROS) generation capability and better adsorption of microorganisms.[4–7] Alternatively, silver is known to exhibit broad-spectrum antibacterial activity against various bacterial species, such as *Escherichia coli* (*E. coli*), *Bacillus subtilis* and *Staphylococcus aureus*, and has been exploited in a variety of applications such as dental wound healing or in catheters.[8,9] Current research has demonstrated that silver nanoagents can have excellent inhibitory bacterial growth concentrations against *E. coli*, down to 0.125 μg mL^{-1}, depending on the size of the nanoparticles (NPs).[10–14] However, the targeted delivery and active transportation of antibacterial nanomaterials remains a big obstacle.

Motile micro/nanomotors have attracted tremendous attention and impart antibacterial agents with active delivery capability and better sterilizing performance by overcoming the passive transportation of nanomaterials and enhancing the corresponding fluid dynamics. By coupling the rapid movement of micromotors with the intrinsic antibacterial activity of enzymes or nanomaterials, various antibacterial microbots

[a]*College of Materials Science and Engineering, Nanjing Tech University, Nanjing 211816, China. E-mail: liuwenjuan@njtech.edu.cn*
[b]*Jiangsu Collaborative Innovation Center for Advanced Inorganic Functional Composites, Nanjing Tech University, Nanjing 211816, China*
[c]*State Key Laboratory of Mechanics and Control of Mechanical Structures, Nanjing University of Aeronautics and Astronautics, Nanjing 210016, China. E-mail: long_8446110@nuaa.edu.cn*

†Electronic supplementary information (ESI) available. See DOI: 10.1039/d0nr06281b

have been successfully developed, promoting the antibacterial agent–bacterial interaction and resulting in greatly enhanced bacteria-killing capability.[10,15–22] Specifically, the introduction of micro/nanomotors as delivery vehicles for Ag or Ag compounds provides an on-the-fly release and enhanced interaction with bacteria. For instance, Pd/Ni/Ag magnetic nanocoil motors exhibit better antibacterial performance and can be magnetically manipulated externally to move freely even at low magnetic fields as compared to Ag nanoparticles only.[10] Ag nanoparticles-coated Janus Mg microbots are able to swim in aqueous media and these self-propelled micromotors exhibit the enhanced capability of capturing and killing bacteria because of the motion-induced solution mixing process and the release of more silver ions.[18,19] Furthermore, light-driven AgCl microstars enable the inhibition of the growth of bacteria owing to the intrinsic bacteriostatic properties of silver ions.[16] Bubble-driven micromotors have been reported to be an effective antibacterial platform due to their intense diffusion ability, simple power input and widespread applications in vast water systems. Manganese dioxide (MnO_2) as an efficient hydrogen peroxide catalyst has recently been constructed into chemically propelled micromotors and has displayed great environmental and biomedical potential by virtue of its low cost, high abundance, superb stability and biocompatibility.[23–27] However, on encountering undesirable highly concentrated oxidative peroxide fuel for propulsion, MnO_2 micromotors require engineering with improved motion performance, along with good antibacterial capability to satisfy the rigorous biological demands where the adopted hydrogen peroxide is quite low.[28] For instance, the concentration of H_2O_2 used in disinfection (usually 0.5–3%) is too high to be suitable for wound treatment; as such, there remains a huge challenge in the rational design of highly efficient antibacterial micromotors with low levels of oxidative fuel concentration.

Herein, bubble-propelled PEDOT/MnO_2@Ag micromotors are proposed to serve as an efficient delivery micro-platform for antibacterial agents by combining their rapid movement with the effective disinfection action of Ag^+ species. This antibacterial micromotor was synthesized by the cathodic co-electrodeposition of MnO_2 and Ag, following a supportive PEDOT outer layer formation, leading to a uniform dispersion of cubic Ag NPs on the inner surface. By finely tuning the co-deposition time, the Ag NPs can nucleate and grow into larger dimensions because of the high deposition efficacy. Due to the synergistic catalytic reaction of both MnO_2 and Ag, the micromotors can rapidly swim in very low concentrations of H_2O_2 and maintain good antibacterial performance from the on-the-fly release of Ag^+ ions. Compared to PEDOT/MnO_2 micromotors, PEDOT/MnO_2@Ag motors propel much faster and kill twice the amount of *E. coli* in 0.2% H_2O_2 solution (bacterial death was 92% *vs.* 43%). Such a dual functional design endows micromotors with attractive propulsion features and contributes to a novel strategy for disinfection applications in the environmental and biomedical fields.

Results and discussion

The new antibiotic-free strategy to combat bacteria, as illustrated in Fig. 1, is based on the strong bactericidal activity of Ag-decorated MnO_2 (PEDOT/MnO_2@Ag) micromotors. This novel antibacterial micromotor was obtained by the cathodic co-electrodeposition of MnO_2 and Ag in the inner walls of Au sputtered polycarbonate membranes, following the initial polymerization of the PEDOT layer.[29] The driving impetus is provided by the MnO_2 catalyst to decompose H_2O_2 and generate intense bubble recoil. Meanwhile, the generation of cubic Ag NPs accelerates the speed of the micromotors and facilitates sterilization, which is attributed to their excellent catalytic ability and unique antibacterial performance. The on-the-fly release of Ag^+ ions and the violent convection induced by the micromotors' motion greatly enhance the bacteria-killing efficacy. Therefore, combining the inherent property of the broad-spectrum antibacterial activity of the nanoagent against bacteria with motile micromotors could pave a new pathway for bacterial disinfection applications.

The morphology and composition of the synthetic PEDOT/MnO_2@Ag micromotors are characterized in Fig. 2. Template-assisted electrodeposition is utilized to obtain such tubular micromotors. Through an electrically conductive PEDOT outer layer, MnO_2 and Ag can be deposited into the inner walls of micro-tubes with cathodic reduction. The basic mechanism of reactions can be explained by the following equations.[30]

$$KMnO_4 + 5e^- + 8H^+ \rightarrow K^+ + Mn^{2+} + 4H_2O \quad (1)$$

$$KMnO_4 + 3e^- + 4H^+ \rightarrow K^+ + MnO_2 + 2H_2O \quad (2)$$

$$KMnO_4 + 3e^- + 2H_2O \rightarrow K^+ + MnO_2 + 4OH^- \quad (3)$$

$$Ag^+ + e^- \rightarrow Ag \quad (4)$$

A small amount of $KMnO_4$ was first reduced to manganese ions (Mn^{2+}) due to the initial weakly acidic conditions. During the reaction, hydrogen protons were consumed and manganese dioxide was formed on the PEDOT substrate, along with the silver deposition. These micromotors possess a completely tubular shape, approximately 15 μm in length and 5 μm in dia-

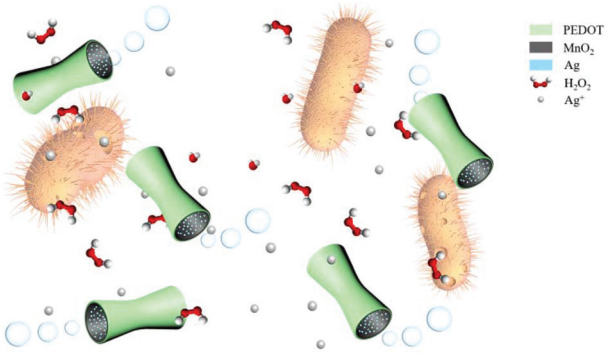

Fig. 1 A schematic diagram of the movement of PEDOT/MnO_2@Ag micromotors and their inhibition effect against bacteria.

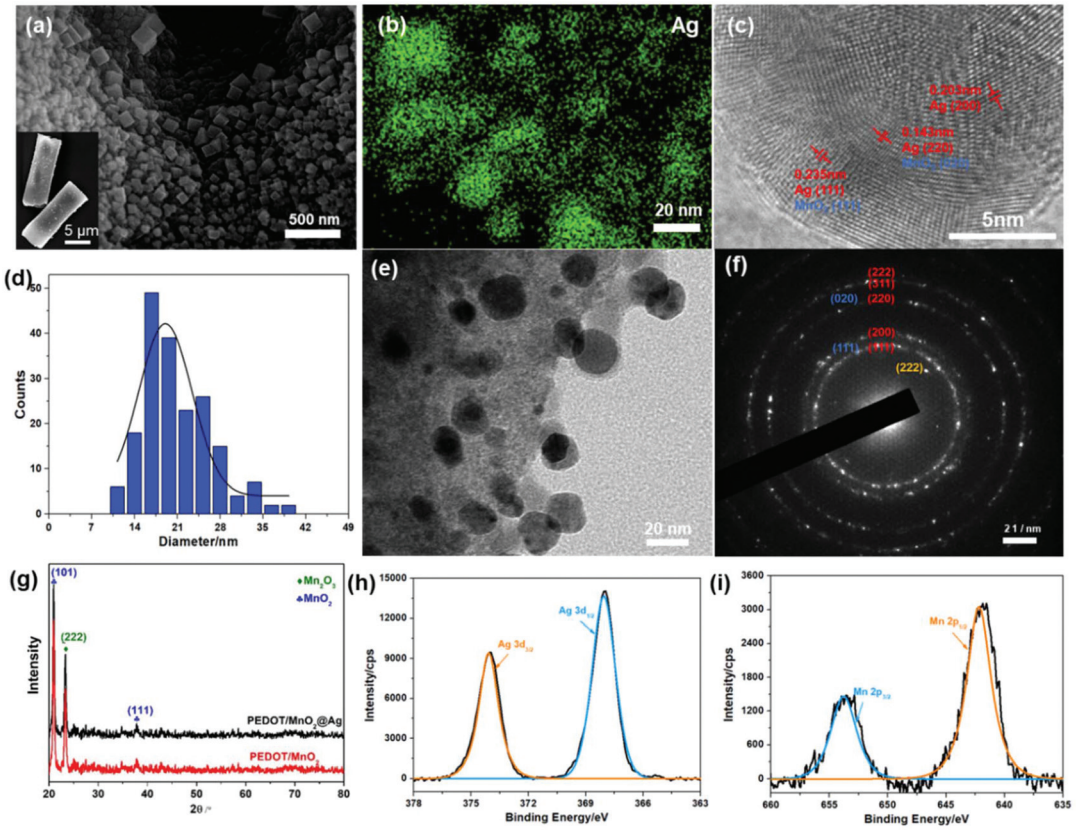

Fig. 2 Characterization of PEDOT/MnO_2@Ag micromotors. SEM images of the inner surface from a PEDOT/MnO_2@Ag microtube and the inset image revealing the whole outer morphology (a). EDS mapping image of the inner surface (b) and its corresponding HR-TEM image (c), size and distribution of nanoparticles (d) and their TEM image (e). SAED of nanoparticles (f), XRD patterns of both PEDOT/MnO_2@Ag and PEDOT/MnO_2 micromotors (g), Ag 3d XPS spectra (h), and Mn 2p XPS spectra (i).

meter, as shown in the smaller illustration in Fig. 2(a). No obviously different appearances were indicated from those micromotors depositing only MnO_2, however, the inner surface of the micromotors attracts great attention. Adequate squares grow on the inner surface when Ag and MnO_2 are co-electrodeposited (Fig. 2(a)), while only rough MnO_2 is present as a consequence of no silver plating, as seen in Fig. S1(a).† EDS mapping in Fig. 2(b) indicates that those tiny cubes are evenly dispersed and are mainly composed of Ag with edges of about 20 nm. Moreover, the morphology of these particles could be partially controlled by the deposition time of the inner layer. When the deposition time is short, for example, 250 s, small particles nucleate and scatter in the inner surface, as illustrated in Fig. S1(b),† similar to the reported pattern of silver deposition.[30,31] With the extension of time from 500 s to 750 s, the particles are converted into crystal squares and grow to larger dimensions of approximately 500 nm in length, and even occupy almost the whole space of the micro-tube, as shown in Fig. S1(c and d),† confirming the favourable effect of deposition time on the growth of nanoparticles. Mn and Ag elements are well distributed (Fig. S2†) and the detailed distribution of the elemental content (Mn, C, O, S and Ag) is shown in Table S1;† no silver was found in PEDOT/MnO_2 micromotors. The amount of Ag in all of the PEDOT/MnO_2@Ag micromotors was slightly higher than that of Mn, and maintained an obvious growth tendency, indicating a greater deposition efficiency, corresponding to the abundant nanoparticles in Fig. S3.† However, if the co-deposition ratio of Ag to MnO_2 was reduced by half of the pre-setting parameter, no obvious cubes were found on the inner surface even with a deposition time of 500 s. A rough inner surface with round nanoparticles was displayed because of not enough Ag to nucleate and grow into cubic structures (Fig. S4†).

The size and distribution of Ag squares were determined. Squares between 16 nm and 25 nm account for the main part in Fig. 2(d), which is consistent with TEM images in Fig. 2(e), and form better crystal structures as compared to silver–graphene oxide nanocomposites.[32] Ag NPs in micromotors with a deposition time of 250 seconds also had a normal distribution, ranging from 10 nm to 20 nm (Fig. S3(a)†). However, the extension of the deposition time to 750 s resulted in greatly varied dimensions of Ag NPs (Fig S3(b)†). Although possessing well-distributed Ag NPs at deposition times of 250 s or 750 s, PEDOT/MnO_2@Ag micromotors deposited for 500 s were chosen as representative owing to the regular pattern and suitable size of the Ag NPs. To further confirm the composition of

the squares, high-resolution transmission electron microscopy (HR-TEM) and selected area electron diffraction (SAED) were carried out (Fig. 2(c) and (f)). Multiple crystal facets of manganese dioxide, such as (020), (111) were explored in the squares in addition to the (111), (200) and (220) facets of silver, indicating the partial participation of MnO_2 in the main Ag squares during the cathodic reduction process. Correspondingly, the TEM elemental mapping results indicated that these nanoparticles contained a large amount of silver, as illustrated in Fig. 2b and S3(e, f),† and the size of nanoparticles was in line with the previous description, with the smaller being around 10 nm, while the big larger was greater than 80 nm.

The XRD results of PEDOT/MnO_2@Ag micromotors are displayed in Fig. 2(g). Compared to PEDOT/MnO_2, no signal of silver was found in Ag-decorated MnO_2 micromotors. The (111) crystal plane of ramsdellite manganese dioxide was indicated in two XRD patterns, corresponding well to the HR-TEM and SAED results. Nevertheless, the (222) crystal plane of manganese(III) sesquioxide occurred in both the XRD and SAED results, which was probably due to the partial dissolution and cathodic reduction of manganese dioxide in lye, as seen in the equation below:

$$MnO_2 + 2e^- + H_2O \rightarrow Mn_2O_3 + 2OH^- \quad (5)$$

The XPS survey further revealed the high-resolution spectra of carbon (C 1s peak), oxygen (O 1s peak), manganese (Mn 2p peak) and silver (Ag 3d peak) in the PEDOT/MnO_2@Ag micromotors, which are in good agreement with the EDS results. The oxidation states of all these elements were characterized, as seen in Fig. 2(h, i) and Fig. S5(b, c).† The peaks at the binding energies of 653.7 eV and 642.2 eV were assigned to Mn_2O_3 and MnO_2, respectively, indicating that the Mn oxides were composed of both trivalent and tetravalent Mn ions. The peaks of the C 1s spectra and O 1s spectra correspond to the binding energies of various functional groups such as C–C/C–H/C=C, C–OH, C=O, and O–C=O, revealing the nature of the covalent bonds of the oxygen and carbon atoms.[33] Oxygen functional groups account for a large proportion of the PEDOT/MnO_2@Ag micromotors, which are provided both by PEDOT and MnO_2. Intriguingly, the Ag spectrum decomposed into two peaks, solely corresponding to the Ag simple substance with $3d_{5/2}$ at 368.1 eV and $2d_{3/2}$ at 374.0 eV. This result elucidates that only the zero valence state of Ag exists in the micromotors, due to the electro-reduction deposition process, which is also in good agreement with a previous report.[34] The alkaline conditions of the plating solution and the cathodic reduction guaranteed that no silver would be further oxidized. Therefore, the XPS spectra further confirmed the elemental constitution and the valence state of the PEDOT/MnO_2@Ag micromotors.

The propulsion performance of the PEDOT/MnO_2@Ag micromotors was experimentally tested in comparison to PEDOT/MnO_2, and their time-lapse tracks are recorded in Fig. 3. Fig. 3a displays the co-dependence of the velocity of PEDOT/MnO_2 and PEDOT/MnO_2@Ag micromotors on the

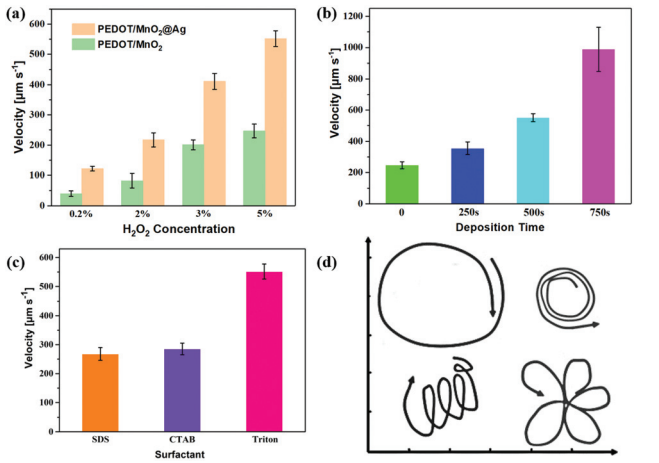

Fig. 3 Kinematic performance of PEDOT/MnO_2@Ag micromotors. (a) The co-dependence of the velocity of PEDOT/MnO_2@Ag micromotors with H_2O_2 concentrations in comparison to PEDOT/MnO_2 motors. (b) The velocity of PEDOT/MnO_2@Ag micromotors with different deposition times in 5% H_2O_2 and 0.167% Triton X-100 solution. (c) The velocity comparison of PEDOT/MnO_2@Ag micromotors with three different surfactants in 5% H_2O_2 solution, and (d) four common tracking trajectories showing the propulsion of PEDOT/MnO_2@Ag micromotors in 5% H_2O_2 and 0.167% Triton X-100 solution; the distance between each small axis is 50 μm.

H_2O_2 concentration. As indicated, the cathodic co-deposition of Ag resulted in a slight decline in MnO_2 (Table S1†), as compared to independently depositing MnO_2 (PEDOT/MnO_2 micromotors). However, the velocity of the micromotors did not decrease accordingly, owing to the existence of silver. As expected, silver has better catalytic activity for hydrogen peroxide than manganese dioxide, leading to enhanced propulsion behavior.[35,36] Correspondingly, the greater the concentration of H_2O_2, the quicker the activated micromotors, as shown in Fig. 3(a) and Video S1.† For instance, the motions of PEDOT/MnO_2@Ag micromotors with 500 seconds deposition can be observed in the peroxide fuel down to the concentration of 0.1%, as seen in Video S2,† which is much lower as compared to our previous work.[27] The synergistic effect between Ag and MnO_2, as well as the large catalytic area offered by the rough inner surface, contributes to its extraordinary high-performance.[37] In contrast, PEDOT/MnO_2 micromotors with the same deposition time required highly concentrated H_2O_2 fuel for propulsion. This clearly illustrates that both micromotors exhibit faster propulsion at higher concentrations of H_2O_2. The speed of PEDOT/MnO_2@Ag micromotors (500 seconds of deposition time) increases from 122 μm s^{-1} to 562 μm s^{-1} upon raising the peroxide level from 0.2% to 5%, showing a tremendous difference in speed as compared to PEDOT/MnO_2, attributed to the existence of abundant Ag NPs for enhancing the catalytic ability.[38] However, once the concentration of H_2O_2 declined to 0.01%, PEDOT/MnO_2@Ag micromotors stood still and did not exhibit locomotion, as illustrated in Fig. S6 and Video S2.† The PEDOT/MnO_2@Ag micromotors displayed enhanced propulsion velocities (355, 562 and 989 μm s^{-1})

from 250 seconds of deposition time to 750 seconds, which was much more violent, as shown in Fig. 3(b) and Video S3.† Nevertheless, the great reduction of the Ag deposition ratio by half of the pre-set parameter led to decreased velocities in different H_2O_2 solutions (Fig. S7 and Video S4†). The PEDOT/MnO_2@Ag micromotors with the half-ratio of Ag were motionless in 0.2% H_2O_2 solution because of the lower content of Ag in the inner surface (5.70 wt% seen in Table S1†). We compared the velocity of PEDOT/MnO_2@Ag micromotors to clarify the significant effect of surfactants (Fig. 3(c) and Video S5†). PEDOT/MnO_2@Ag micromotors exhibited better motivation with the assistance of Triton-X100, which is a non-ionic surfactant, as compared to the cationic surfactant CTAB and anionic surfactant SDS. The tracking trajectories in Fig. 3(d) (taken from Videos S1 and S3†) show that the PEDOT/MnO_2@Ag micromotors mainly displayed curve movements,[39] whether orbital, rotary, helical, or curvilinear. According to our previous work on chemically-driven tubular micromotors,[23] the versatile microstructural design of tubular micromotors, as well as catalytic machine power, would contribute to the complicated motion trajectories. Due to the violent bubble ejection and the irregular tube shape, an anisotropic distribution of the drag forces was generated around our PEDOT/MnO_2@Ag micromotor and led to complicated motion patterns rather than a regular linear trajectory. Because of the free-swimming strategy, the control of the motion direction is not essential here; however, it could be regulated by a magnetic field after incorporating the magnetic coating for further target capture, delivery, and killing.[10,40,41] The association of ultrasound with chemically-driven micromotors will give distinct motility, such as group assembly and ultrafast zigzag motion,[42] therefore, leading to concentrated liberated ions in localized regions and a rapid mass transfer. Typically, these bubble-propelled micromotors could result in a violent mixture in the localized-region and ought to accelerate the mass transfer. Thus, chemically driven PEDOT/MnO_2@Ag micromotors are becoming a flexible measure for the rapid elimination of bacteria.

To analyze the motivation modality of the PEDOT/MnO_2@Ag micromotors, we assumed that each complex motion was from the same basic mode, namely, short-range translational motion. This motion is closely dependent on the port orientation of the micromotors. One flat-bottom-type micromotor was numerically simulated using the COMSOL Multiphysics software (COMSOL, Stockholm, Sweden). The tested locomotion velocity generated by bubble propulsion, which was set to the bottom side of the micromotors, was selected as the boundary conditions for calculating the flow field distribution. As illustrated in Fig. 4(a), there were two symmetrical ambient flow vortices around the micromotor, which means that the flow resistances at both sides were identical. Such simulation of the flow field generated by a micromotor illustrates the significantly faster fluid flow near the end side in units of velocity.[43] As a result, the micromotor will theoretically demonstrate a linear motion, agitating the mass translation and mixture in a certain range on its propelling route. However, the solution is not static and any disturbance

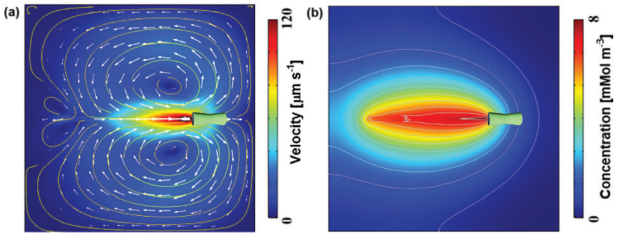

Fig. 4 Simulation of the velocity field (a) and concentration distribution of Ag^+ (b) produced by the PEDOT/MnO_2@Ag micromotor in the presence of 0.2% H_2O_2 fuel.

will change the direction of motion of the micromotor. The imperfect shapes and unevenly distributed catalysts in the inner surface also influenced the propulsion trajectories.[23] Thus, the curve paths of the micromotors are commonly seen, as partially shown in Fig. 3(d). Furthermore, the numerical simulation confirmed the maximum velocity of the PEDOT/MnO_2@Ag micromotors could achieve 120 μm s^{-1} in the center of the 0.2% H_2O_2 solution, which is consistent with our experimental results. The concentration distribution of Ag^+ produced by the PEDOT/MnO_2@Ag micromotor was also simulated. There was a concentration gradient of silver ions in the reverse direction of the micromotor, as seen in Fig. 4(b). As reported,[44] the distribution of Ag^+ will change because of the interactions of micromotors nearby and will finally be uniform throughout the solution after the continuous movement of micromotors.

We then studied the antibacterial capability of PEDOT/MnO_2@Ag micromotors. *E. coli* was used here as the model bacteria as they are common and well-studied. Different control experiments were carried out to demonstrate the efficiency of Ag decoration. During the disinfection process, PEDOT/MnO_2@Ag micromotors were freely swimming in the 0.2% H_2O_2 solution and interacted with *E. coli*. Simultaneously, Ag^+ ions were produced because of the silver corrosion in the H_2O_2 solution.[45] The superoxide radicals ($O_2^{\bullet}$) were also generated from the chemical reaction of $Ag + 2H_2O_2 \rightarrow Ag^+ + O_2^{\bullet} + H_2O$. As reported,[46–48] silver ions and $O_2^{\bullet}$ radicals are responsible for bacterial destruction. By combining the self-propulsion, these PEDOT/MnO_2@Ag micromotors provide ideal biocompatible micro-platforms for the removal of bacteria. After the micromotors propelled and killed bacteria in solution, they were imaged using fluorescence viability studies and compared to the control groups. Fig. 5 shows the antibacterial capability of different micromotors. Both the static PEDOT/MnO_2@Ag and stand-still PEDOT/MnO_2 micromotors were not able to kill bacteria as expected because they cannot set off free elemental Ag or generate reactive oxygen species (ROS) which are harmful to bacteria. Nevertheless, the release of silver ions from moving PEDOT/MnO_2@Ag micromotors could bind to the bacterial membrane, DNA and proteins and lead to lysis, blocking the cell metabolism and replication.[49] At the same time, Ag^+ can penetrate the bacterial cell membrane and induce the generation and accumulation of

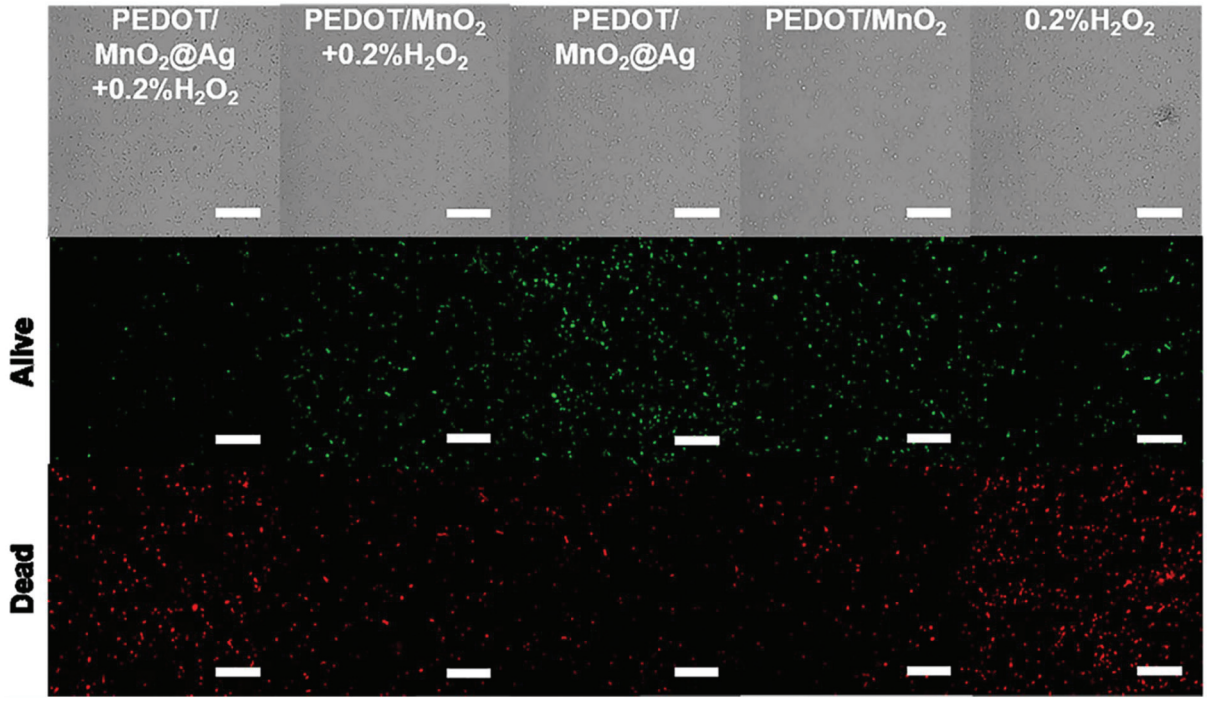

Fig. 5 Bactericidal assay results using PEDOT/MnO_2@Ag micromotors and control samples. Optical microscope images of bacteria using fluorescence lamp after the bactericidal assay. The scale bar is 50 μm.

ROS in cells, and the bacterial inhibition by Ag^+ ion correlated well with the intracellular ROS concentrations.[50] Moreover, with the propulsion of micromotors, the increased localized concentration of Ag^+ would result in an increase in the ROS amount,[51–54] leading to an enhanced apoptosis effect. Currently, fluorescence probes (such as DCFH-DA and CellROX™ Deep Red) are used to detect the generation and accumulation of ROS in cells;[52,55] however, the simultaneous fluorescence emission from the fuel of H_2O_2 prevents further detection. Nevertheless, the overall antibacterial tests have proved the beneficial effects of PEDOT/MnO_2@Ag micromotors. Correspondingly, the percentage of dead *E. coli* in the presence of two types of micromotors and bulk hydrogen peroxide solution was displayed. Generally, H_2O_2 can produce ROS to penetrate the cell membrane and kill bacteria[13] but its high concentration is a big restriction to biological applications.

As illustrated in Fig. 5 and Fig. 6(a), PEDOT/MnO_2 micromotors along with 0.2% H_2O_2 were able to kill around 42% of bacteria, while less than 80% bacterial death occurred with simply 0.2% H_2O_2; the big difference is due to the consumption of oxidative H_2O_2. However, the interaction of bacteria with intense liberated Ag^+ ions in the mixture leads to increased bactericidal activity. Thus, a higher antibacterial effect was observed when the bacteria were in contact with moving PEDOT/MnO_2@Ag micromotors, which were able to kill more than 90% of *E. coli*. Meanwhile, static PEDOT/MnO_2 and PEDOT/MnO_2@Ag micromotors could kill a few bacteria, with death ratios of about 20%. H_2O_2 specifically contributed

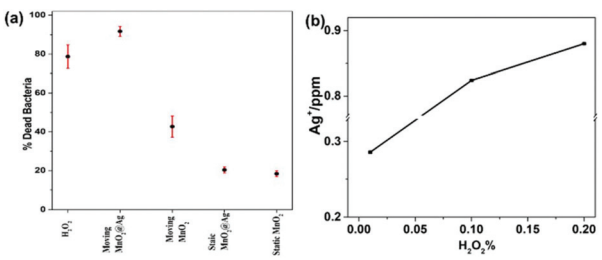

Fig. 6 Percentage of dead *E. coli*. *E. coli*, as model bacteria, are in contact with 0.25 mg of micromotors for 10 min (a) and the released Ag^+ concentration in different H_2O_2 solutions (b).

to the antibacterial activity,[56] suggesting that catalytic oxidation is the main mechanism in the bactericidal process. An increase in bacterial death of about 14% was demonstrated with propelled PEDOT/MnO_2@Ag micromotors and confirmed the positive effects of released Ag^+ ions when considering the consumed H_2O_2. As reported, the minimum inhibitory concentration (MIC) of Ag^+ was significant and was dependent on the bacterial colonies and environmental factors.[57] According to the results of inductively coupled plasma optical emission spectrometry (ICP-OES), the concentration of released Ag^+ ions was 8.8 μMol L^{-1} (about 0.8 μg mL^{-1}) in 0.2% H_2O_2 (Fig. 6b), approaching the previously reported minimum inhibitory concentration (MIC) of Ag^+ (0.50 μg mL^{-1}).[57] However, Ag^+ accumulation would induce certain cytotoxicity in some cells and organs.[58,59] A notable health effect of argyria may occur

when there is a large open wound and large amounts of silver ions are used for dressing.[60] Accordingly, PEDOT/MnO_2@Ag micromotors with large ratios of Ag were not considered to avoid the release of extensive Ag^+ in the surface disinfection and water disinfection applications. The low ratio of Ag deposition (reduced by half concentration in plating solution) released Ag^+ ions of 0.011 μg mL^{-1}, much lower than the reported MIC, along with the motionlessness. Thus, neither high nor low ratios of Ag deposition were adopted for effective and safe antibacterial tests. The influence of H_2O_2 concentration on the killing efficiency of bacteria was also studied (Fig. S8†). The percentage of dead *E. coli* bacteria sharply decreased to nearly 5% in the presence of PEDOT/MnO_2@Ag micromotors with 0.1% H_2O_2. Although the concentration of released Ag^+ ions was 8.2 μMol L^{-1}, similar to that in 0.2% H_2O_2 (Fig. 6b), the significantly reduced H_2O_2 resulted in poor bactericidal performance, indicating that the liberated Ag^+ could not compensate for the oxidative action of H_2O_2 in the bacterial killing process. Therefore, the concentration of H_2O_2 should be carefully determined because of its dual roles as both fuel and oxidative agent. Electrostatic attraction is supposed to compensate for the lower antibacterial capability caused by undesirable reduced H_2O_2, once the outer layer of MnO_2@Ag micromotors is decorated with a positively charged surface in the future (for instance a positively charged poly (allylamine hydrochloride) or chitosan coating).[61,62]

Experimental

Materials and reagents

Potassium nitrate (KNO_3), sodium dodecyl sulfate (SDS), hexadecyl trimethyl ammonium bromide (CTAB), silver nitrate ($AgNO_3$), potassium permanganate ($KMnO_4$), methylene chloride (CH_2Cl_2), ethanol (C_2H_5OH), and hydrogen peroxide (30% H_2O_2) (Cat. 7722-84-1) were all purchased from Sinopharm Chemical Reagents Co. Ltd. 3,4-Ethylenedioxythiophene (EDOT) and polyethylene glycol octyl phenyl ether (Triton X-100) were obtained from Alfa Aesar Chemical Regent Co. Ltd. Polycarbonate (PC) membranes (Catalog no. 7060-2513) with an average pore diameter of 5 μm were purchased from Whatman Inc., NY, USA. All reagents were of analytical grade and were used as received without further treatment.

Fabrication of PEDOT/MnO_2@Ag micromotors

The PEDOT/MnO_2@Ag micromotors were fabricated using a template-directed electrochemical deposition protocol. The PC membrane was employed as the template. A thin gold film (approximately 40 nm) was first deposited on one side of the porous membrane to serve as the working electrode using a EMACE200 sputter coater. The evaporation deposition was performed under a high vacuum below 7×10^{-2} mBar at a current of 40 mA after evacuated twice and the deposition time was 160 seconds. A large stainless steel plate with an area of 25 cm^2 and Ag/AgCl with 3 M KCl were used as the counter electrode and reference electrode, respectively. The membrane was then assembled in a self-designed plating cell with a stainless steel foil serving as a contact for the working electrode. Electrodeposition was carried out using a CHI 660E electrochemical workstation (CH Instruments. Ins, Shanghai, China). First, the poly(3,4-ethylenedioxythiophene) (PEDOT) layer was electropolymerized at +1.0 V from a plating solution containing 15 mM EDOT, 7.5 mM KNO_3 and 100 mM SDS, with a total charge of 0.3 C (a platinum wire was utilized as a counter electrode). Subsequently, a mixed solution containing 4 mM $AgNO_3$ and 20 mM $KMnO_4$ was prepared as the electrolyte for the inner MnO_2@Ag layer electrochemical growth, applying −1.0 mA current with 500 seconds of deposition, as well as 250 seconds and 750 seconds for comparison. The low ratio of Ag deposition was conducted in a plating solution containing 2 mM $AgNO_3$ and 20 mM $KMnO_4$ with 500 s deposition time. Afterwards, alumina slurry (average diameter of 5 μm) was used to remove the sputtered gold layer by hand polishing. The PC templates were then dissolved in methylene chloride for more than 10 min to set off the micromotors, along with slight shaking. The latter were collected by centrifugation at 7000 rpm for 3 min and washed 3 times each with methylene chloride, ethanol and deionized water, with a 3 min centrifugation after each wash. Centrifugation was carried out using an H/T18MM centrifuge (HX Instruments. Ins, Hunan, China). All the micromotors were stored in ultrapure water at room temperature for further use.

Characterization of micromotors

The morphologies and element distributions of the micromotors were determined using a JSM-7600F Scanning Electron Microscope (SEM), with an acceleration voltage of 15 kV, equipped with an Oxford X-MAX Energy Dispersive X-ray Spectrometer (EDS). The detailed characterization was performed by a Jeol Transmission Electron Microscope (TEM) (Jem-3200FS). An X-ray diffractometer with a CuKα X-ray source (ARL X'TRA) was employed to characterize the crystal structure of the micromotors. X-ray photoelectron spectroscopy (XPS) was carried out using a Kratos AXIS Ultra DLD system with monochromatic Al-Kα X-rays at a photon energy of 1486.7 eV under a base pressure less than 8×10^{-9} mBar. The spectra were acquired with the pass energy of 40 eV and fitted using the XPS PEAK41 software. Optical microscopy images and motion videos of the micromotors in different H_2O_2 solutions were recorded by an inverted optical microscope (CKX53, Olympus Instrument Inc., Tokyo, Japan) coupled with 20× and 40× microscope objectives and an Olympus digital camera (DP74, Olympus Instrument Inc., Japan). The concentration of Ag^+ ions contained in the mixture was determined by Inductively Coupled Plasma Optical Emission Spectrometry (Agilent 5110) and fluorescence confocal images were recorded by a laser scanning confocal microscope (LSCM) (LEIKA DB6000 B).

COMSOL simulation of Ag^+ concentration

For COMSOL analysis, the fluid–structure interaction (FSI) module combined with the transport of diluted spaces (TDS)

module was chosen to analyze the ion concentration distribution released by PEDOT/MnO_2@Ag micromotors. A Two-dimensional model of the liquid surroundings was built with a PEDOT/MnO_2@Ag micromotor placed inside. The moving speed obtained from the experimental results was applied to the micromotor in the FSI module for calculating the motion-induced liquid flow, which then influenced the ion concentration around the micromotor during the motion. The flux discontinuity in the TDS module, utilized to represent the ion release, was applied to the right part of the micromotor. Time-dependent studies were computed with the time arrangement of 0.5 s and the time step of 0.01 s.

Inductively coupled plasma optical emission spectrometry (ICP-OES) measurement

Each aliquot of 0.25 mg of PEDOT/MnO_2@Ag micromotors (half batch) was placed in a 1.5 ml Eppendorf centrifuge tube for 10 min, which contained a total of 1 ml of solution. The concentrations of the H_2O_2 solutions were 0.01%, 0.1% and 0.2%. The mixture was then centrifuged at 10 000 rpm for 3 minutes to remove the motor and the obtained supernatant was tested by ICP-OES. The assay was carried out in triplicate (n = 3) for 10 minutes.

Antibacterial test

Once the PEDOT/MnO_2@Ag micromotors were characterized and weighed, their bactericidal activity was tested. Each aliquot of 0.25 mg of PEDOT/MnO_2@Ag micromotors (half batch) was placed in Petri dishes containing a total of 1 ml of bacteria (10 million per mL) in H_2O_2 solution. The assay was carried out in triplicate (n = 3) for 10 minutes. Micromotors were removed from the solution after centrifugation at 10 000 rpm. The bacteria present in the solution and attached to micromotors were washed and re-suspended in fresh deionized water. According to the procedures in the living/dead bacteria survival kit, the samples were mixed with 6 μM STYO 9 or 30 μM propidium iodide. Afterwards, they were centrifuged at 10 000 rpm after being placed in the dark for 15 minutes and were again dispersed in deionized water and immediately imaged using a fluorescence microscope. The percentage of cell viability was defined as the total number of live cells divided by the sum of live and dead cells using Image J software. PEDOT/MnO_2 micromotors and bulk H_2O_2 solution were utilized as the control. The amount of these micromotors was kept the same for each experimental group.

Conclusions

We have presented the use of bubble-propelled PEDOT/MnO_2@Ag micromotors as an efficient antibiotic-free strategy to combat bacteria. The antibacterial micromotors were synthesized by a simple cathodic co-electrodeposition of Ag and MnO_2, which are respectively responsible for the bacterial killing and propulsion force. The size and distribution of bactericidal Ag NPs on the inner surface could be tailored by changing the deposition time. Perfect Ag nanosquares with 20 nm diameter were obtained under 500 s deposition, which grew to larger dimensions upon increasing the deposition time. In addition to sterilization, Ag NPs can accelerate the speed of micromotors due to their excellent catalytic ability to H_2O_2. Consequently, the PEDOT/MnO_2@Ag micromotors fuelled by only 0.2% H_2O_2 could achieve efficient motion with a velocity of up to 122 μm s^{-1}, as compared to the lower speed (40 μm s^{-1}) of PEDOT/MnO_2 micromotors. The continuous motion of bubble-driven micromotors coupled with the sterilization of released Ag^+ led to enhanced motor–bacterial interaction and bacterial killing capability. More than 90% of *E. coli* were killed with PEDOT/MnO_2@Ag micromotors in 0.2% H_2O_2 for 10 minutes. However, significantly reduced H_2O_2 fuel resulted in poor bactericidal performance, indicating that the liberated Ag^+ could not compensate for the oxidative action of H_2O_2 in the bactericidal process. Overall, our results provide additional information for designing micromotor-based antibacterial micro-platforms propelled by hydrogen peroxide, where the influence of oxidative hydrogen peroxide is rarely explored in antibacterial micromotors.

Conflicts of interest

All authors declare no conflicts of interest.

Acknowledgements

This work was supported by the National Natural Science Foundation of China (No. 51975278), Natural Science Foundation of Jiangsu Province (BK20181292 and BK20180698), the Nanjing Tech University Supported Program, the PAPD-A Project Funded by the Priority Academic Program Development of Jiangsu Higher Education Institutions, the Research Fund of State Key Laboratory of Mechanics and Control of Mechanical Structures (Nanjing University of Aeronautics and Astronautics) (Grant No. MCMS-I-0318Y01). The authors acknowledge Suqian Advanced Materials Industry Technology Innovation Center of Nanjing Tech University for support.

Notes and references

1 K. E. Jones, N. G. Patel, M. A. Levy, A. Storeygard, D. Balk, J. L. Gittleman and P. Daszak, *Nature*, 2008, **451**, 990–993.
2 R. L. Siegel, K. D. Miller and A. Jemal, *CA-Cancer J. Clin.*, 2019, **69**, 7–34.
3 G. V. Vimbela, S. M. Ngo, C. Fraze, L. Yang and D. A. Stout, *Int. J. Nanomed.*, 2017, **12**, 3941–3965.
4 M. Parlinska-Wojtan, M. Kus-Liskiewicz, J. Depciuch and O. Sadik, *Bioprocess Biosyst. Eng.*, 2016, **39**, 1213–1223.
5 N. Salah, S. S. Habib, Z. H. Khan, A. Memic, A. Azam, E. Alarfaj, N. Zahed and S. Al-Hamedi, *Int. J. Nanomed.*, 2011, **6**, 863–869.

6 A. Hatamie, A. Khan, M. Golabi, A. P. F. Turner, V. Beni, W. C. Mak, A. Sadollahkhani, H. Alnoor, B. Zargar, S. Bano, O. Nur and M. Willander, *Langmuir*, 2015, **31**, 10913–10921.
7 M. R. Bindhu, M. Umadevi, M. K. Micheal, M. V. Arasu and N. A. Al-Dhabi, *Mater. Lett.*, 2016, **166**, 19–22.
8 M. Rai, A. Yadav and A. Gade, *Biotechnol. Adv.*, 2009, **27**, 76–83.
9 K. Yuan, Z. Jiang, B. Juradosanchez and A. Escarpa, *Chem. – Eur. J.*, 2020, **26**, 2309–2326.
10 M. Hoop, Y. Shen, X. Chen, F. Mushtaq, L. M. Iuliano, M. S. Sakar, A. Petruska, M. J. Loessner, B. J. Nelson and S. Pané, *Adv. Funct. Mater.*, 2016, **26**, 1063–1069.
11 D. Vilela, M. M. Stanton, J. Parmar and S. Sánchez, *ACS Appl. Mater. Interfaces*, 2017, **9**, 22093–22100.
12 G. Franci, A. Falanga, S. Galdiero, L. Palomba, M. Rai, G. Morelli and M. Galdiero, *Molecules*, 2015, **20**, 8856–8874.
13 K. Tahir, S. Nazir, B. Li, A. U. Khan, Z. U. H. Khan, A. Ahmad, Q. U. Khan and Y. Zhao, *J. Photochem. Photobiol., B*, 2015, **153**, 261–266.
14 M. Smekalova, V. Aragon, A. Panacek, R. Prucek, R. Zboril and L. Kvitek, *Vet. J.*, 2016, **209**, 174–179.
15 M. Kiristi, V. V. Singh, B. E. De Ávila, M. Uygun, F. Soto, D. A. Uygun and J. Wang, *ACS Nano*, 2015, **9**, 9252–9259.
16 J. Simmchen, A. Baeza, A. Miguel-Lopez, M. M. Stanton, M. Vallet-Regi, D. Ruiz-Molina and S. Sánchez, *ChemNanoMat*, 2017, **3**, 65–71.
17 J. Li, V. Singh, S. Sattayasamitsathit, J. Orozco, K. Kaufmann, R. Dong, W. Gao, B. Jurado-Sánchez, Y. Fedorak and J. Wang, *ACS Nano*, 2014, **8**, 11118–11125.
18 Y. Ge, M. Liu, L. Liu, Y. Sun, H. Zhang and B. Dong, *Nano-Micro Lett.*, 2016, **8**, 157–164.
19 D. Vilela, M. M. Stanton, J. Parmar and S. Sánchez, *ACS Appl. Mater. Interfaces*, 2017, **9**, 22093–22100.
20 T. Xu, W. Gao, L. Xu, X. Zhang and S. Wang, *Adv. Mater.*, 2017, **29**, 1603250.
21 Y. Xing, Q. Pan, X. Du, T. Xu, Y. He and X. Zhang, *Appl. Mater. Today*, 2019, **17**, 85–91.
22 Y. Xing, M. Zhou, X. Du, X. Li, J. Li, T. Xu and X. Zhang, *ACS Appl. Mater. Interfaces*, 2019, **11**, 10426–10433.
23 W. Liu, H. Ge, X. Chen, X. Lu, Z. Gu, J. Li and J. Wang, *ACS Appl. Mater. Interfaces*, 2019, **11**, 16164–16173.
24 H. Wang, G. J. Zhao and M. Pumera, *J. Am. Chem. Soc.*, 2014, **136**, 2719–2722.
25 M. Safdar, T. D. Minh, N. Kinnunen and J. Jänis, *ACS Appl. Mater. Interfaces*, 2016, **8**, 32624–32629.
26 K. Villa, J. Parmar, D. Vilela and S. Sánchez, *ACS Appl. Mater. Interfaces*, 2018, **10**, 20478–20486.
27 W. Liu, H. Ge, Z. Gu, X. Lu, J. Li and J. Wang, *Small*, 2018, **14**, 1802771.
28 G. Yang, L. Xu, Y. Chao, J. Xu, X. Sun, Y. Wu, R. Peng and Z. Liu, *Nat. Commun.*, 2017, **8**, 1–13.
29 W. Gao, S. Sattayasamitsathit, J. Orozco and J. Wang, *J. Am. Chem. Soc.*, 2011, **133**, 11862–11864.
30 Y. Wang and I. Zhitomirsky, *Mater. Lett.*, 2011, **65**, 1759–1761.
31 B. Song, C. Zhang, G. Zeng, J. Gong, Y. Chang and Y. Jiang, *Arch. Biochem. Biophys.*, 2016, **604**, 167–176.
32 S. Khorrami, Z. Abdollahi, G. Eshaghi, A. Khosravi, E. Bidram and A. Zarrabi, *Sci. Rep.*, 2019, **9**, 1–10.
33 L. H. Tjeng, M. B. J. Meinders, J. van Elp, J. Ghijsen and G. A. Sawatzky, *Phys. Rev. B: Condens. Matter Mater. Phys.*, 1990, **41**, 3190.
34 H. Ye, J. Kang, G. F. Ma, H. Q. Sun and S. B. Wang, *J. Colloid Interface Sci.*, 2018, **528**, 271–280.
35 H. Wang, G. J. Zhao and M. Pumera, *J. Am. Chem. Soc.*, 2014, **136**, 2719–2722.
36 W. Z. Teo, H. Wang and M. Pumera, *Chem. Commun.*, 2016, **52**, 4333–4336.
37 Y. Wang, C. C. Mayorga-Martinez, J. G. S. Moo and M. Pumera, *ACS Appl. Energy Mater.*, 2018, **1**, 3443–3448.
38 F. Soto, M. A. Lopez-Ramirez, I. Jeerapan, B. E. De Avila, R. K. Mishra, X. L. Lu, I. Chai, C. R. Chen, D. Kupor, A. Nourhani and J. Wang, *Adv. Funct. Mater.*, 2019, **29**, 1900658.
39 S. C. Edberg, E. W. Rice, R. J. Karlin and M. J. Allen, *J. Appl. Microbiol.*, 2000, **88**, 106S–116S.
40 M. Zhou, T. Hou, J. Li, S. Yu, Z. Xu, M. Yin, J. Wang and X. Wang, *ACS Nano*, 2019, **13**, 1324–1332.
41 J. Orozco, G. Pan, S. Sattayasamitsathit, M. Galarnyk and J. Wang, *Analyst*, 2015, **140**, 1421–1427.
42 X. Lu, H. Shen, Y. Wei, H. Ge, J. Wang, H. Peng and W. Liu, *Small*, 2020, 2003678.
43 M. Rai, S. Deshmukh, A. P. Ingle and A. Gade, *J. Appl. Microbiol.*, 2012, **112**, 841–852.
44 C. Chen, X. Chang, H. Teymourian, D. E. RamÍrez-Herrera, B. E. D. Ávila, X. Lu, J. Li, S. He, C. Fang, Y. Liang, F. Mou, J. Guan and J. Wang, *Angew. Chem., Int. Ed.*, 2018, **57**, 241–245.
45 D. He, S. Garg and T. D. Waite, *Langmuir*, 2012, **28**, 10266–10275.
46 Z. Xiu, Q. Zhang, H. L. Puppala, V. L. Colvin and P. J. J. Alvarez, *Nano Lett.*, 2012, **12**, 4271–4275.
47 Q. Xin, H. Shah, A. Nawaz, W. J. Xie, M. Z. Akram, A. Batool, L. Q. Tian, S. U. Jan, R. Baddula, B. D. Guo, Q. Liu and G. R. Gong, *Adv. Mater.*, 2019, **31**, 1804838.
48 V. Vedarethinam, L. Huang, W. Xu, R. Zhang, D. D. Guraw, X. M. Sun, J. Yang, R. P. Chen and K. Qian, *Small*, 2019, **15**, 1803051.
49 L. E. García González, M. N. Macgregor, R. M. Visalakshan, N. Ninan, A. A. Cavallaro, A. D. Trinidad, Y. P. Zhao, A. J. D. Hayballcdf and K. Vasilev, *Chem. Commun.*, 2019, **55**, 171–174.
50 O. Choi and Z. Hu, *Environ. Sci. Technol.*, 2008, **42**, 4583–4588.
51 J. S. Kim, E. Kuk, K. N. Yu, J. H. Kim, S. J. Park, H. J. Lee, S. H. Kim, Y. K. Park, Y. H. Park, C. Y. Hwang, Y. K. Kim, Y. S. Lee, D. H. Jeong and M. H. Cho, *Nanomed.-Nanotechnol. Biol. Med.*, 2007, **3**, 95–101.
52 R. Zhao, M. Lv, Y. Li, M. Sun, W. Kong, L. Wang, S. Song, C. Fan, L. Jia, S. Qiu, Y. Sun, H. Song and R. Hao, *ACS Appl. Mater. Interfaces*, 2017, **9**, 15328–15341.
53 O. Choi and Z. Hu, *Environ. Sci. Technol.*, 2008, **42**, 4583–4588.

54 B. Ramalingam, T. Parandhaman and S. K. Das, *ACS Appl. Mater. Interfaces*, 2016, **8**, 4963–4976.
55 G. Yang, M. Fan, J. Zhu, C. Ling, L. Wu, X. Zhang, M. Zhang, J. Li, Q. Yao, Z. Gu and X. Cai, *Biomaterials*, 2020, **255**, 120155.
56 L. Wang, H. He, Y. B. Yu, L. Sun, S. J. Liu, C. B. Zhang and L. He, *J. Inorg. Biochem.*, 2014, **135**, 45–53.
57 T. J. Berger, J. A. Spadaro, S. E. Chapin and R. O. Becker, *Antimicrob. Agents Chemother.*, 1976, **9**, 357–358.
58 H. T. Ratte, *Environ. Toxicol. Chem.*, 1999, **18**, 89–108.
59 M. Rai, A. Yadav and A. Gade, *Biotechnol. Adv.*, 2009, **27**, 76–83.
60 P. L. Drake and K. J. Hazelwood, *Ann. Occup. Hyg.*, 2005, **49**, 575–585.
61 T. Li, L. Li, W. Song, L. Wang, G. Shao and G. Zhang, *ECS J. Solid State Sci. Technol.*, 2015, **4**, S3016–S3019.
62 Z. Wu, Y. Wu, W. He, X. Lin, J. Sun and Q. He, *Angew. Chem., Int. Ed.*, 2013, **52**, 7000–7003.